



7

Analysis of Texture

Texture is one of the important characteristics of images.

We find around us several examples of texture:
on wood, cloth, brick walls, floors, etc.

We may group texture into two general categories:
(quasi-) periodic and random.



If there is a repetition of a texture element at almost regular or (quasi-) periodic intervals, we may classify the texture as being (quasi-) periodic or ordered;

the elements of such a texture are called textons or textels.

Brick walls and floors with tiles are examples of periodic texture.



On the other hand, if no texton can be identified, such as in clouds and cement-wall surfaces, we can say that the texture is random.

Rao gives a more detailed classification, including weakly ordered or oriented texture that takes into account hair, wood grain, and brush strokes in paintings.

Texture may also be related to visual and/or tactile sensations such as fineness, coarseness, smoothness, granularity, periodicity, patchiness, being mottled, or having a preferred orientation.

According to Haralick et al., texture relates to information about the spatial distribution of gray-level variation.



7.1 Texture in Biomedical Images

A wide variety of texture is encountered in biomedical images.

Oriented texture is common in medical images due to the fibrous nature of muscles and ligaments, as well as the extensive presence of networks of blood vessels, veins, ducts, and nerves.

A preferred or dominant orientation is associated with the functional integrity and strength of such structures.

Ordered texture is often found in images of the skins of reptiles, the retina, the cornea, the compound eyes of insects, and honeycombs.



Organs such as the liver are made up of clusters of parenchyma that are of the order of $1 - 2 \text{ mm}$ in size.

The pixels in CT images have a typical resolution of $1 \times 1 \text{ mm}$, which is comparable to the size of the parenchymal units.

With ultrasonic imaging, the wavelength of the probing radiation is of the order of $1 - 2 \text{ mm}$, which is also comparable to the size of parenchymal clusters.

Under these conditions, the liver appears to have a speckled random texture.

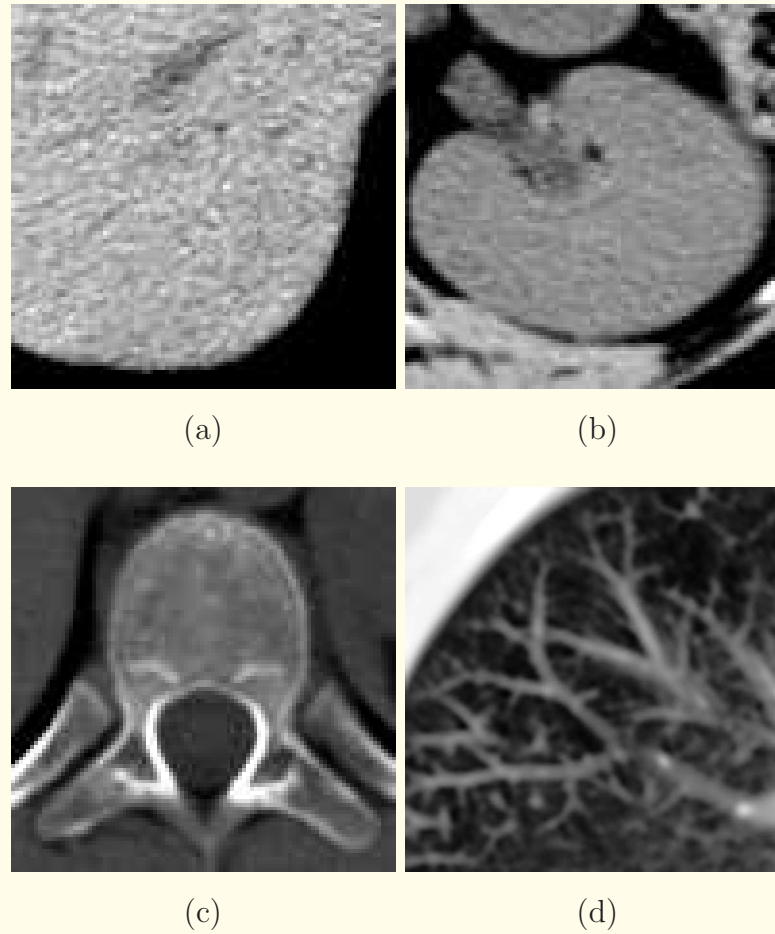


Figure 7.1: Examples of texture in CT images: (a) Liver. (b) Kidney. (c) Spine. (d) Lung. The true size of each image is $55 \times 55 \text{ mm}$. The images represent widely differing ranges of tissue density, and have been enhanced to display the inherent texture. Image data courtesy of Alberta Children's Hospital.

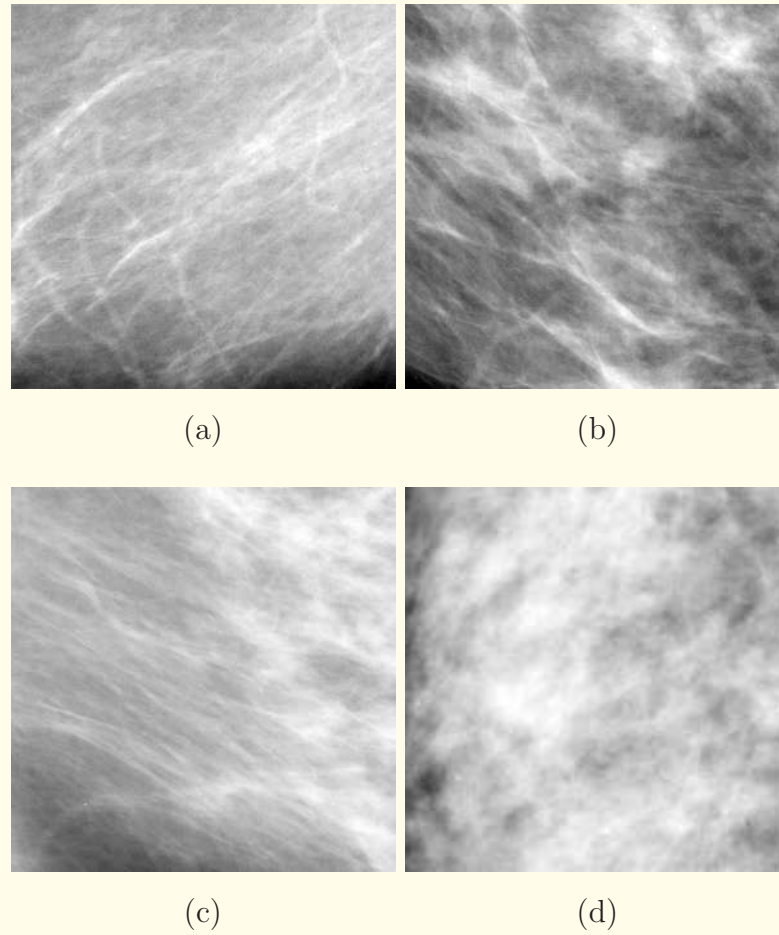


Figure 7.2: Examples of texture in mammograms (from the MIAS database): (a) – (c) oriented texture; true image size $60 \times 60 \text{ mm}$; (d) random texture; true image size $40 \times 40 \text{ mm}$.

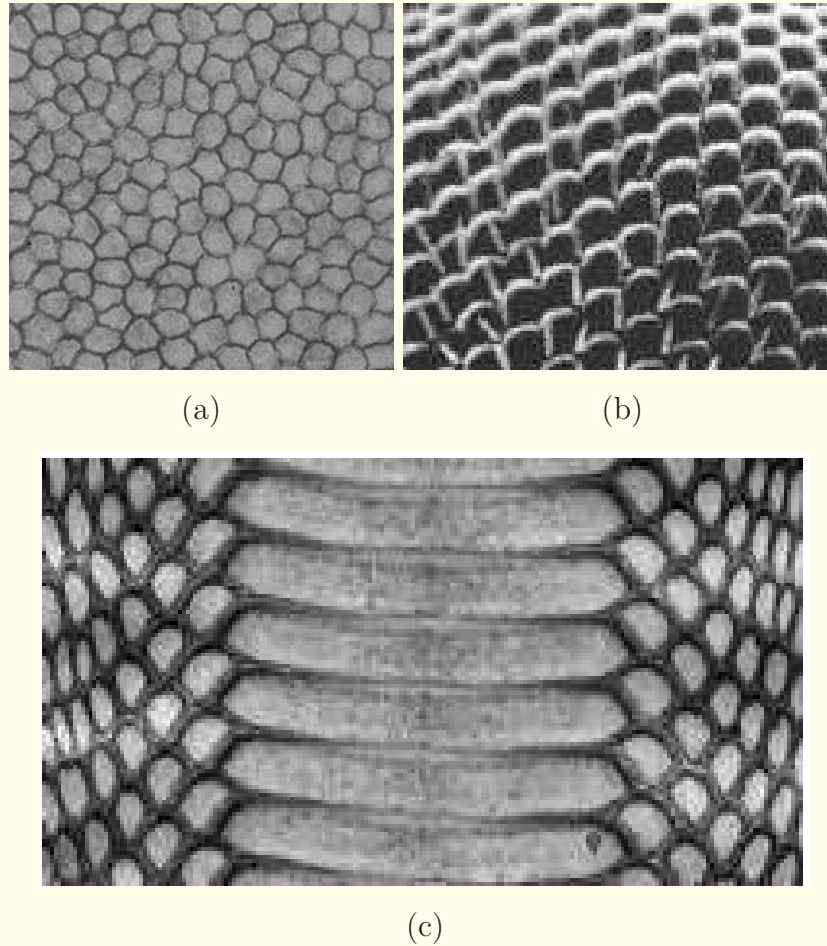


Figure 7.3: Examples of ordered texture: (a) Endothelial cells in the cornea. Image courtesy of J. Jaroszewski. (b) Part of a fly's eye. Reproduced with permission from D. Suzuki, "Behavior in drosophila melanogaster: A geneticist's view", *Canadian Journal of Genetics and Cytology*, XVI(4): 713 – 735, 1974. © Genetics Society of Canada. (c) Skin on the belly of a cobra snake. Image courtesy of Implora, Colonial Heights, VA. <http://www.implora.com>. See also Figure 1.5.



7.2 Models for the Generation of Texture

There are similarities between speech and texture generation.

Types of sounds produced by the human vocal system:

voiced, unvoiced, and plosive sounds.

The first two types of speech signals may be modeled as the convolution of an input excitation signal with a filter function.

The excitation signal is quasi-periodic when we use the vocal cords to create voiced sounds,

or random in the case of unvoiced sounds.

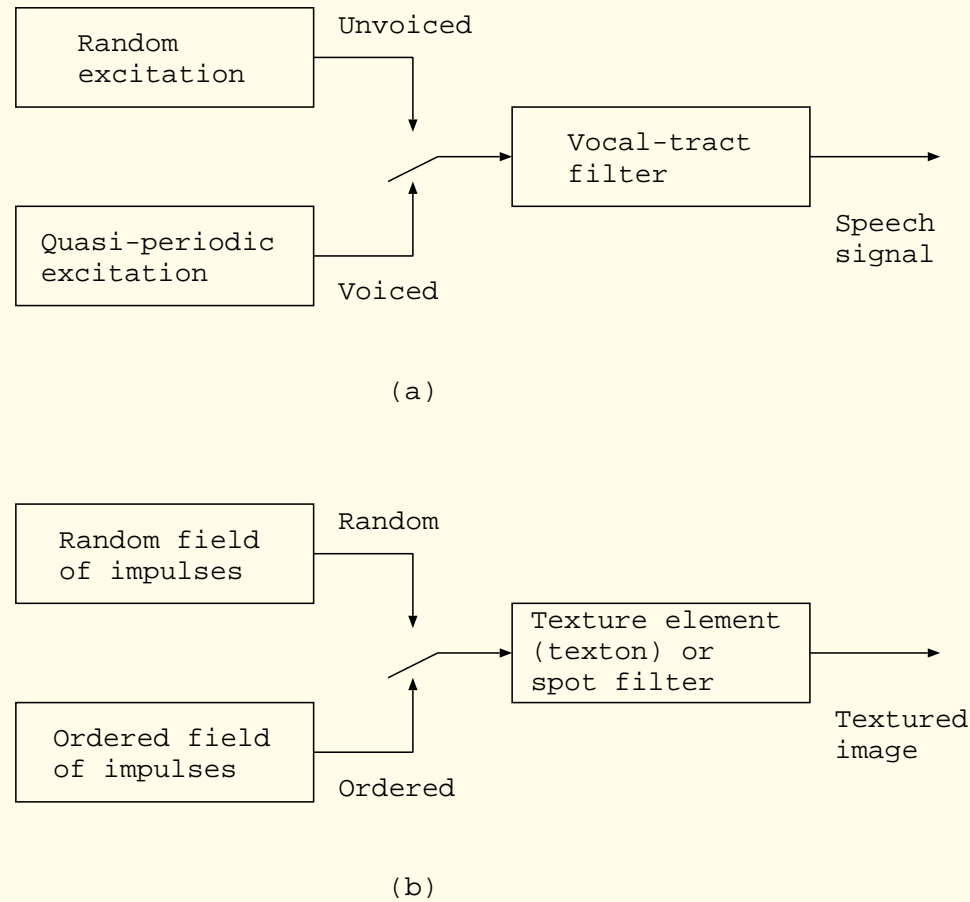


Figure 7.4: (a) Model for speech signal generation. (b) Model for texture synthesis. Reproduced with permission from A.C.G. Martins, R.M. Rangayyan, and R.A. Ruschioni, "Audification and sonification of texture in images", *Journal of Electronic Imaging*, 10(3): 690 – 705, 2001. © SPIE and IS&T.



Texture may also be modeled as the convolution of an input impulse field with a spot or a texton that would act as a filter.

The “spot noise” model of van Wijk for synthesizing random texture uses this model:

the Fourier spectrum of the spot acts as a filter that modifies the spectrum of a 2D random-noise field.



Ordered texture may be generated by specifying the basic pattern or texton to be used, and a placement rule.

The placement rule may be expressed as a field of impulses.

Texture is then given by the convolution of the impulse field with the texton, which could also be represented as a filter.



7.2.1 *Random texture*

Random texture may be modeled as a filtered version of a field of white noise, where the filter is represented by a spot of a certain shape and size (much smaller than the image).

The 2D spectrum of the noise field, which is essentially a constant, is shaped by the 2D spectrum of the spot.

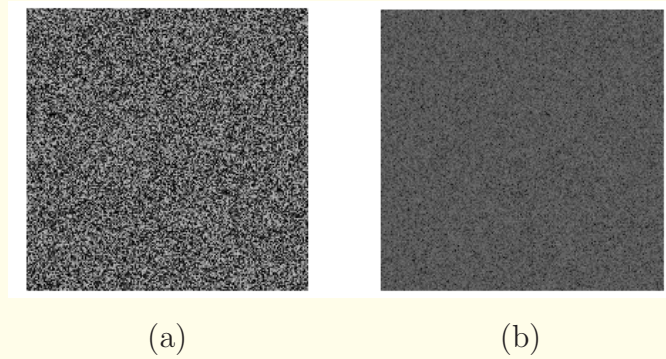
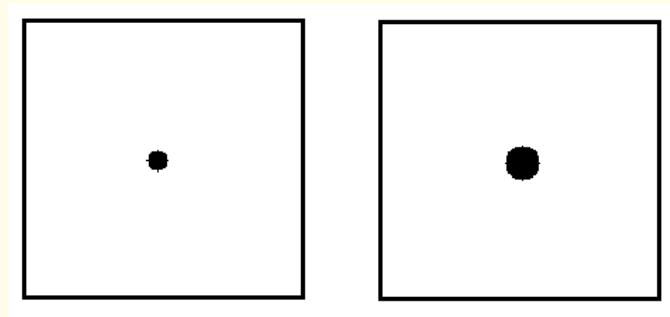
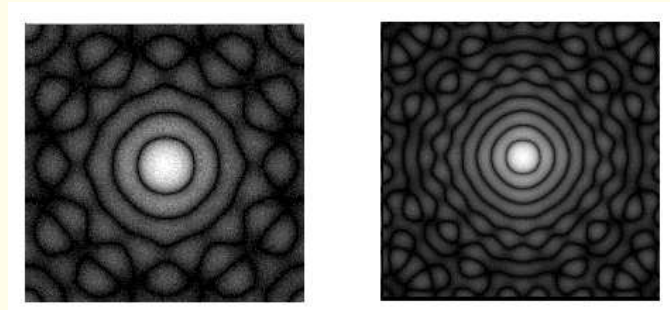


Figure 7.5: (a) Image of a random-noise field (256×256 pixels). (b) Spectrum of the image in (a). Reproduced with permission from A.C.G. Martins, R.M. Rangayyan, and R.A. Ruschioni, “Audification and sonification of texture in images”, *Journal of Electronic Imaging*, 10(3): 690 – 705, 2001. © SPIE and IS&T.



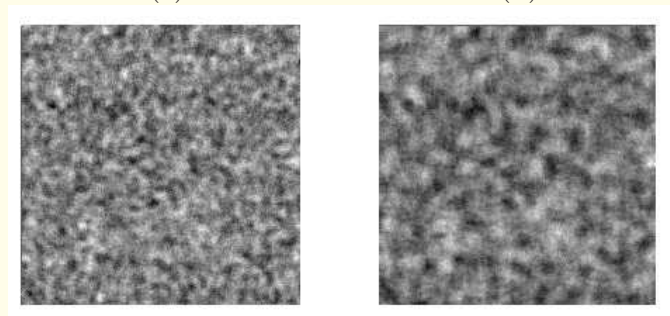
(a)

(b)



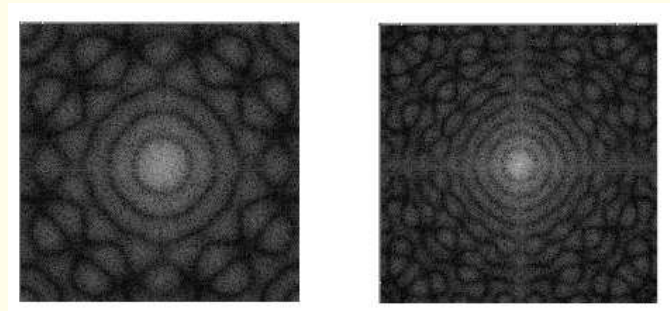
(c)

(d)



(e)

(f)



(g)

(h)



Figure 7.6: (a) Circle of diameter 12 pixels. (b) Circle of diameter 20 pixels. (c) Fourier spectrum of the image in (a). (d) Fourier spectrum of the image in (b). (e) Random texture with the circle of diameter 12 pixels as the spot. (f) Random texture with the circle of diameter 20 pixels as the spot. (g) Fourier spectrum of the image in (e). (h) Fourier spectrum of the image in (f). The size of each image is 256×256 pixels. Reproduced with permission from A.C.G. Martins, R.M. Rangayyan, and R.A. Ruschioni, “Audification and sonification of texture in images”, *Journal of Electronic Imaging*, 10(3): 690 – 705, 2001. © SPIE and IS&T.

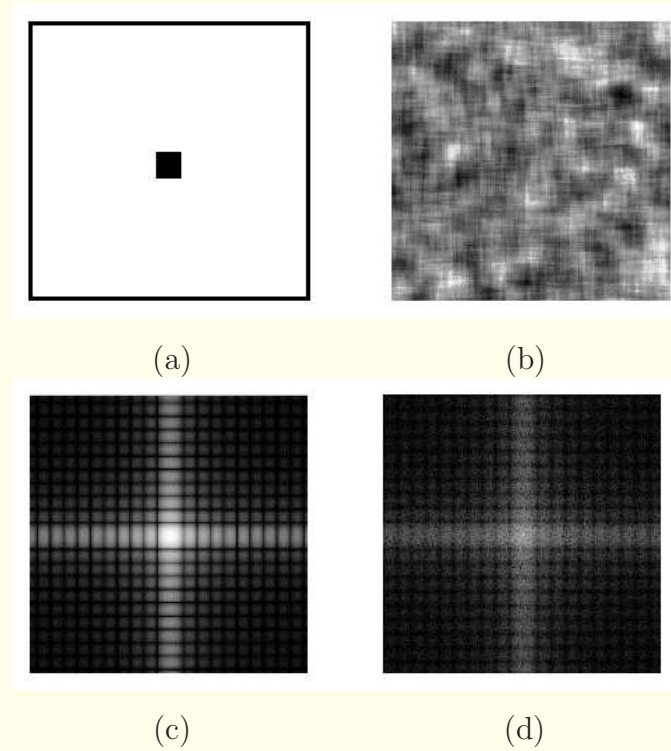


Figure 7.7: (a) Square of side 20 pixels. (b) Random texture with the square of side 20 pixels as the spot. (c) Spectrum of the image in (a). (d) Spectrum of the image in (b). The size of each image is 256×256 pixels. Reproduced with permission from A.C.G. Martins, R.M. Rangayyan, and R.A. Ruschioni, “Audification and sonification of texture in images”, *Journal of Electronic Imaging*, 10(3): 690 – 705, 2001. © SPIE and IS&T.

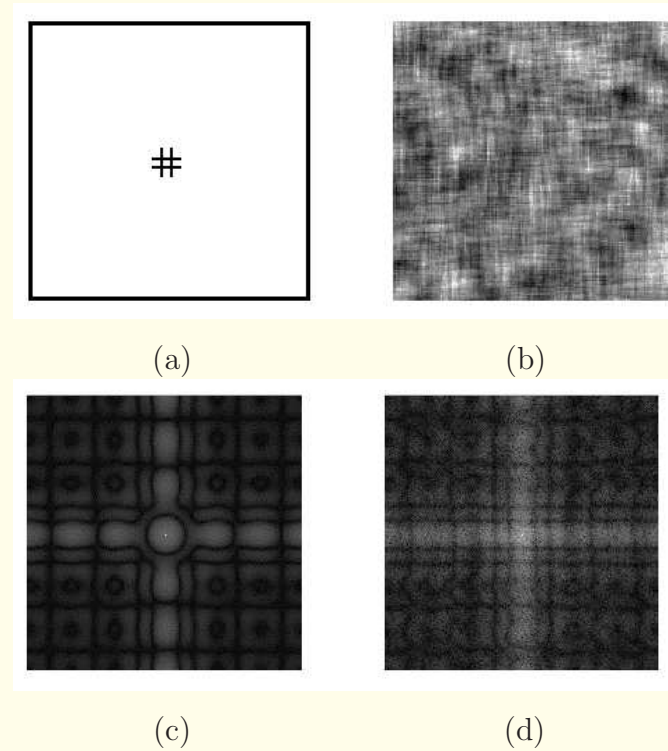


Figure 7.8: (a) Hash of side 20 pixels. (b) Random texture with the hash of side 20 pixels as the spot. (c) Spectrum of the image in (a). (d) Spectrum of the image in (b). The size of each image is 256×256 pixels. Reproduced with permission from A.C.G. Martins, R.M. Rangayyan, and R.A. Ruschioni, “Audification and sonification of texture in images”, *Journal of Electronic Imaging*, 10(3): 690 – 705, 2001. © SPIE and IS&T.



7.2.2 Ordered texture

Ordered texture may be modeled as the placement of a basic pattern or texton (of a much smaller size than the image) at positions determined by a 2D field of (quasi-) periodic impulses.

The separations between the impulses in the x and y directions determine the periodicity or “pitch” in the two directions.

This process may also be modeled as the convolution of the impulse field with the texton.



The difference between ordered and random texture lies in the structure of the impulse field:

the former uses a (quasi-) periodic field of impulses,
the latter uses a random-noise field.

The spectral characteristics of the texton could be seen as a filter that modifies the spectrum of the impulse field (which is essentially a 2D field of impulses as well).

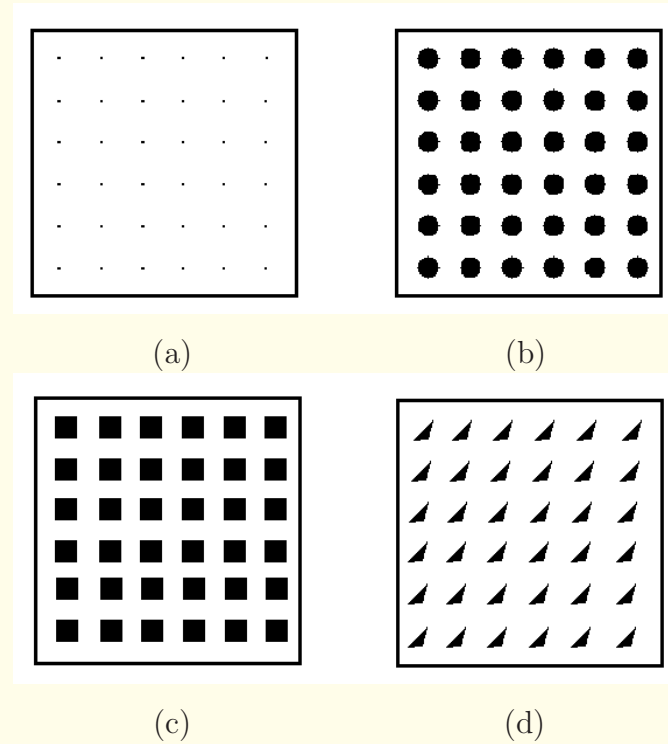


Figure 7.9: (a) Periodic field of impulses with $p_x = 40$ pixels and $p_y = 40$ pixels. (b) Ordered texture with a circle of diameter 20 pixels, $p_x = 40$ pixels, and $p_y = 40$ pixels as the spot. (c) Ordered texture with a square of side 20 pixels, $p_x = 40$ pixels, and $p_y = 40$ pixels as the spot. (d) Ordered texture with a triangle of sides 12, 16, and 23 pixels as the spot; $p_x = 40$ pixels; and $p_y = 40$ pixels. The size of each image is 256×256 pixels. Reproduced with permission from A.C.G. Martins, R.M. Rangayyan, and R.A. Ruschioni, “Audification and sonification of texture in images”, *Journal of Electronic Imaging*, 10(3): 690 – 705, 2001. © SPIE and IS&T.



7.2.3 *Oriented texture*

Images with oriented texture may be generated using the spot-noise model by providing line segments or oriented motifs as the spot.

The preferred orientation of the texture and the directional concentration of the energy are evident in the Fourier domain.

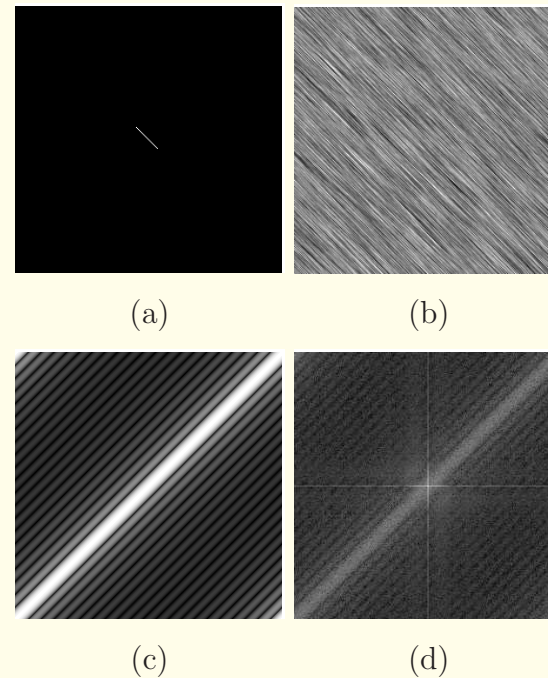


Figure 7.10: Example of oriented texture generated using the spot-noise model in Figure 7.4: (a) Spot with a line segment oriented at 135° . (b) Oriented texture generated by convolving the spot in (a) with a random-noise field. (c) and (d) Log-magnitude Fourier spectra of the spot and the textured image, respectively. The size of each image is 256×256 pixels.



7.3 Statistical Analysis of Texture

Measures of texture may be derived based upon the moments of the gray-level PDF (or normalized histogram) of the given image.

The k^{th} central moment of the PDF $p(l)$ is defined as

$$m_k = \sum_{l=0}^{L-1} (l - \mu_f)^k p(l), \quad (7.1)$$

where $l = 0, 1, 2, \dots, L - 1$ are the gray levels in the image f , and μ_f is the mean gray level of the image given by

$$\mu_f = \sum_{l=0}^{L-1} l p(l). \quad (7.2)$$



The second central moment or variance of the gray levels is

$$\sigma_f^2 = m_2 = \sum_{l=0}^{L-1} (l - \mu_f)^2 p(l), \quad (7.3)$$

and can serve as a measure of inhomogeneity.



The normalized third and fourth moments, known as the skewness and kurtosis, respectively, and defined as

$$skewness = \frac{m_3}{m_2^{3/2}}, \quad (7.4)$$

$$kurtosis = \frac{m_4}{m_2^2}, \quad (7.5)$$

indicate the asymmetry and uniformity of the PDF.

High-order moments are affected significantly by noise or error in the PDF, and may not be reliable features.



Byng et al. computed the skewness of the histograms of 24×24 (3.12×3.12 *mm*) sections of mammograms.

An average skewness measure was computed for each image by averaging the section-based skewness measures of the image.

Mammograms of breasts with increased fibroglandular density were observed to have histograms skewed toward higher density, resulting in negative skewness.

Mammograms of fatty breasts tended to have positive skewness.

The skewness measure was found to be useful in predicting the risk of development of breast cancer.



7.3.1 *The gray-level co-occurrence matrix*

Given the general description of texture as a pattern of the occurrence of gray levels in space, the most commonly used measures of texture, in particular of random texture, are the statistical measures proposed by Haralick et al.

Haralick's measures are based upon the moments of a joint PDF that is estimated as the joint occurrence or co-occurrence of gray levels, known as the gray-level co-occurrence matrix (GCM).

GCMs, also known as spatial gray-level dependence (SGLD) matrices, may be computed for various orientations and distances.



GCM $P_{(d, \theta)}(l_1, l_2)$ = probability of occurrence of the pair of gray levels (l_1, l_2) separated by a given distance d at angle θ .

GCMs are constructed by mapping the gray-level co-occurrence counts or probabilities based on the spatial relations of pixels at different angular directions (specified by θ) while scanning the image from left-to-right and top-to-bottom.

Due to the fact that neighboring pixels in natural images tend to have nearly the same values, GCMs tend to have large values along and around the main diagonal,

and low values away from the diagonal.



For an image with B *b/pixel*, there will be $L = 2^B$ gray levels;

the GCM is of size $L \times L$.

For an image quantized to 8 *b/pixel*, there are 256 gray levels, and the GCM is of size 256×256 .

Fine quantization to large numbers of gray levels, such as $2^{12} = 4,096$ levels in high-resolution mammograms, will increase the size of the GCM to unmanageable levels,

and also reduce the values of the entries in the GCM.

It may be advantageous to reduce the number of gray levels to a relatively small number before computing GCMs.



A reduction in the number of gray levels with smoothing can also reduce the effect of noise on the statistics computed from GCMs.

GCMs are commonly formed for unit pixel distances and the four angles of 0° , 45° , 90° , and 135° .

(Strictly speaking, the distances to the diagonally connected neighboring pixels at 45° and 135° is $\sqrt{2} \times$ pixel size.)



1	1	1	1	1	1	1	1	1	1	2	3	2	2	1	2
0	1	1	1	1	1	1	1	1	1	1	2	2	3	4	5
1	0	0	0	1	1	1	1	1	1	1	1	2	2	4	6
2	2	3	5	4	3	1	0	1	1	1	1	1	2	3	5
4	6	5	4	3	1	1	2	2	1	1	1	1	1	2	4
5	5	2	1	2	3	2	2	2	3	3	4	3	2	1	3
4	3	1	2	1	1	1	2	2	2	1	2	2	2	3	5
2	0	2	0	1	3	1	3	5	3	3	2	2	3	3	6
1	1	2	2	1	2	1	2	3	3	3	4	4	6	5	6
1	1	2	4	1	0	0	1	3	4	5	5	5	4	4	6
1	1	1	4	2	1	2	3	5	5	5	4	4	3	4	6
1	1	1	4	4	4	5	6	6	5	4	3	2	3	5	6
1	1	2	5	5	4	5	5	4	3	3	2	3	4	5	6
2	1	4	5	5	5	5	4	3	1	1	1	4	6	5	6
2	2	5	5	5	4	3	2	2	1	1	4	6	6	6	7
4	4	4	4	3	2	2	1	0	1	5	6	6	6	6	7

Figure 7.11: A 16×16 part of the image in Figure 2.1 (a) quantized to 3 b/pixel , shown as an image and as a 2D array of pixel values.



Table 7.1: Gray-level Co-occurrence Matrix for the Image in Figure 7.11, with the Second Pixel Immediately Below the First.

Current Pixel	Next Pixel Below							
	0	1	2	3	4	5	6	7
0	0	3	4	1	0	1	0	0
1	6	44	10	9	5	1	0	0
2	3	13	13	5	8	3	1	0
3	1	5	11	5	3	5	2	0
4	0	1	5	7	5	9	3	0
5	0	0	1	5	11	10	4	0
6	0	0	0	0	2	3	10	1
7	0	0	0	0	0	0	0	1

Pixels in the last row were not processed. The GCM has not been normalized.



7.3.2 Haralick's measures of texture

Based upon normalized GCMs, Haralick et al. proposed several quantities as measures of texture.

$$p(l_1, l_2) = \frac{P(l_1, l_2)}{\sum_{l_1=0}^{L-1} \sum_{l_2=0}^{L-1} P(l_1, l_2)}. \quad (7.6)$$

$$p_x(l_1) = \sum_{l_2=0}^{L-1} p(l_1, l_2), \quad (7.7)$$

$$p_y(l_2) = \sum_{l_1=0}^{L-1} p(l_1, l_2), \quad (7.8)$$



$$p_{x+y}(k) = \underbrace{\sum_{l_1=0}^{L-1} \sum_{l_2=0}^{L-1}}_{l_1+l_2=k} p(l_1, l_2), \quad (7.9)$$

where $k = 0, 1, 2, \dots, 2(L-1)$, and

$$p_{x-y}(k) = \underbrace{\sum_{l_1=0}^{L-1} \sum_{l_2=0}^{L-1}}_{|l_1-l_2|=k} p(l_1, l_2), \quad (7.10)$$

where $k = 0, 1, 2, \dots, L-1$.



The energy feature F_1 , which is a measure of homogeneity, is

$$F_1 = \sum_{l_1=0}^{L-1} \sum_{l_2=0}^{L-1} p^2(l_1, l_2). \quad (7.11)$$

A homogeneous image has a small number of entries along the diagonal of the GCM with large values: large F_1 .

An inhomogeneous image will have small values spread over a larger number of GCM entries: low F_1 .



The contrast feature, F_2 , is defined as

$$F_2 = \sum_{k=0}^{L-1} k^2 \underbrace{\sum_{l_1=0}^{L-1} \sum_{l_2=0}^{L-1}}_{|l_1-l_2|=k} p(l_1, l_2). \quad (7.12)$$

The correlation measure, F_3 , which represents linear dependencies of gray levels, is defined as

$$F_3 = \frac{1}{\sigma_x \sigma_y} \left[\sum_{l_1=0}^{L-1} \sum_{l_2=0}^{L-1} l_1 l_2 p(l_1, l_2) - \mu_x \mu_y \right], \quad (7.13)$$

where μ_x and μ_y are the means, and σ_x and σ_y are the standard deviation values of p_x and p_y , respectively.



Sum of squares:

$$F_4 = \sum_{l_1=0}^{L-1} \sum_{l_2=0}^{L-1} (l_1 - \mu_f)^2 p(l_1, l_2), \quad (7.14)$$

where μ_f is the mean gray level of the image.

Inverse difference moment, a measure of local homogeneity:

$$F_5 = \sum_{l_1=0}^{L-1} \sum_{l_2=0}^{L-1} \frac{1}{1 + (l_1 - l_2)^2} p(l_1, l_2). \quad (7.15)$$



Sum average:

$$F_6 = \sum_{k=0}^{2(L-1)} k p_{x+y}(k). \quad (7.16)$$

Sum variance:

$$F_7 = \sum_{k=0}^{2(L-1)} (k - F_6)^2 p_{x+y}(k). \quad (7.17)$$



Sum entropy:

$$F_8 = - \sum_{k=0}^{2(L-1)} p_{x+y}(k) \log_2 [p_{x+y}(k)] . \quad (7.18)$$

Entropy, a measure of nonuniformity in the image or the complexity of the texture:

$$F_9 = - \sum_{l_1=0}^{L-1} \sum_{l_2=0}^{L-1} p(l_1, l_2) \log_2 [p(l_1, l_2)] . \quad (7.19)$$



The difference variance measure F_{10} is defined as the variance of p_{x-y} , in a manner similar to that given by Equations 7.16 and 7.17 for its sum counterpart.

The difference entropy measure is defined as

$$F_{11} = - \sum_{k=0}^{L-1} p_{x-y}(k) \log_2 [p_{x-y}(k)] . \quad (7.20)$$



Two information-theoretic measures of correlation:

$$F_{12} = \frac{H_{xy} - H_{xy1}}{\max\{H_x, H_y\}}, \quad (7.21)$$

$$F_{13} = \{1 - \exp[-2(H_{xy2} - H_{xy})]\}^{\frac{1}{2}}; \quad (7.22)$$



$H_{xy} = F_9$; H_x and H_y are the entropies of p_x and p_y ;

$$H_{xy1} = - \sum_{l_1=0}^{L-1} \sum_{l_2=0}^{L-1} p(l_1, l_2) \log_2 [p_x(l_1) p_y(l_2)]; \quad (7.23)$$

$$H_{xy2} = - \sum_{l_1=0}^{L-1} \sum_{l_2=0}^{L-1} p_x(l_1) p_y(l_2) \log_2 [p_x(l_1) p_y(l_2)]. \quad (7.24)$$



The maximal correlation coefficient feature F_{14} is defined as the square root of the second largest eigenvalue of \mathbf{Q} , where

$$\mathbf{Q}(l_1, l_2) = \sum_{k=0}^{L-1} \frac{p(l_1, k) p(l_2, k)}{p_x(l_1) p_y(k)}. \quad (7.25)$$



If the dependence of texture upon angle is not of interest, GCMs over all angles may be averaged into a single GCM.

The distance d should be chosen taking into account the sampling interval (pixel size) and the size of the texture units of interest.

Some of the features defined above have values much greater than unity, whereas some of the features have values far less than unity.

Normalization to a predefined range, such as $[0, 1]$, over the dataset to be analyzed, may be beneficial.



Parkkinen et al. studied the problem of detecting periodicity in texture using statistical measures of association and agreement.

If the displacement and orientation (d, θ) match the same parameters of the texture, the GCM has large values along the diagonal corresponding to the gray levels in the texture elements.

A measure of association is the χ^2 statistic

$$\chi^2 = \sum_{l_1=0}^{L-1} \sum_{l_2=0}^{L-1} \frac{[p(l_1, l_2) - p_x(l_1) p_y(l_2)]^2}{p_x(l_1) p_y(l_2)}. \quad (7.26)$$

The measure may be normalized by dividing by L ; it is expected to possess a high value for periodic texture as above.



Parkkinen et al. discussed limitations of χ^2 in the analysis of periodic texture, and proposed a measure of agreement:

$$\kappa = \frac{P_o - P_c}{1 - P_c}, \quad (7.27)$$

$$P_o = \sum_{l=0}^{L-1} p(l, l), \quad (7.28)$$

$$P_c = \sum_{l=0}^{L-1} p_x(l) p_y(l). \quad (7.29)$$

κ has its maximal value of unity when the GCM is a diagonal matrix, which indicates perfect agreement or periodic texture.



Chan et al. found the three features of correlation, difference entropy, and entropy to perform better than other combinations of one to eight features selected in a specific sequence.

Sahiner et al. defined a “rubber-band straightening transform” (RBST) to map ribbons around breast masses in mammograms into rectangular arrays (see Figure 7.26), and then computed Haralick’s measures of texture.

Mudigonda et al. computed Haralick’s measures using adaptive ribbons of pixels extracted around mammographic masses, and used the features to distinguish malignant tumors from benign masses; see Sections 7.9 and 8.8.



7.4 Laws' Measures of Texture Energy

Laws proposed a method for classifying each pixel in an image based upon measures of local “texture energy”.

The texture energy features represent the amounts of variation within a sliding window applied to several filtered versions of the given image.

The filters are specified as separable 1D arrays for convolution with the image being processed.



$$\begin{aligned}L3 &= \begin{bmatrix} 1 & 2 & 1 \end{bmatrix}, \\E3 &= \begin{bmatrix} -1 & 0 & 1 \end{bmatrix}, \\S3 &= \begin{bmatrix} -1 & 2 & -1 \end{bmatrix}.\end{aligned}\tag{7.30}$$

The operators $L3$, $E3$, and $S3$ perform center-weighted averaging, symmetric first differencing (edge detection), and second differencing (spot detection), respectively.



Nine 3×3 masks may be generated by multiplying the transposes of the three operators (represented as vectors) with their direct versions.

The result of $L3^T E3$ gives one of the 3×3 Sobel masks.

Operators of length five pixels may be generated by convolving the $L3$, $E3$, and $S3$ operators in various combinations.



$$L5 = L3 * L3 = \begin{bmatrix} 1 & 4 & 6 & 4 & 1 \end{bmatrix},$$

$$E5 = L3 * E3 = \begin{bmatrix} -1 & -2 & 0 & 2 & 1 \end{bmatrix},$$

$$S5 = -E3 * E3 = \begin{bmatrix} -1 & 0 & 2 & 0 & -1 \end{bmatrix}, \quad (7.31)$$

$$R5 = S3 * S3 = \begin{bmatrix} 1 & -4 & 6 & -4 & 1 \end{bmatrix},$$

$$W5 = -E3 * S3 = \begin{bmatrix} -1 & 2 & 0 & -2 & 1 \end{bmatrix},$$

where $*$ represents 1D convolution.

The operators listed above perform the detection of the following types of features: $L5$ – local average; $E5$ – edges; $S5$ – spots; $R5$ – ripples; and $W5$ – waves.



In the analysis of texture in 2D images, the 1D convolution operators given above are used in pairs to achieve various 2D convolution operators:

$$L5L5 = L5^T L5, \quad L5E5 = L5^T E5, \quad \dots,$$

each of which may be represented as a 5×5 array or matrix.

Following the application of the selected filters, texture energy measures are derived from each filtered image by computing the sum of the absolute values in a sliding window.



All of the filters listed above, except $L5$, have zero mean, and hence the texture energy measures derived from the filtered images represent measures of local deviation or variation.

The result of the $L5$ filter may be used for normalization with respect to luminance and contrast.

Feature vectors composed of the values of various Laws' operators for each pixel may be used for classifying the image into texture categories on a pixel-by-pixel basis.

The results may be used for texture segmentation and recognition.

Miller and Astley used features of mammograms based upon the $R5R5$ operator, and obtained an accuracy of 80.3% in the segmentation of the nonfat (glandular) regions in mammograms.

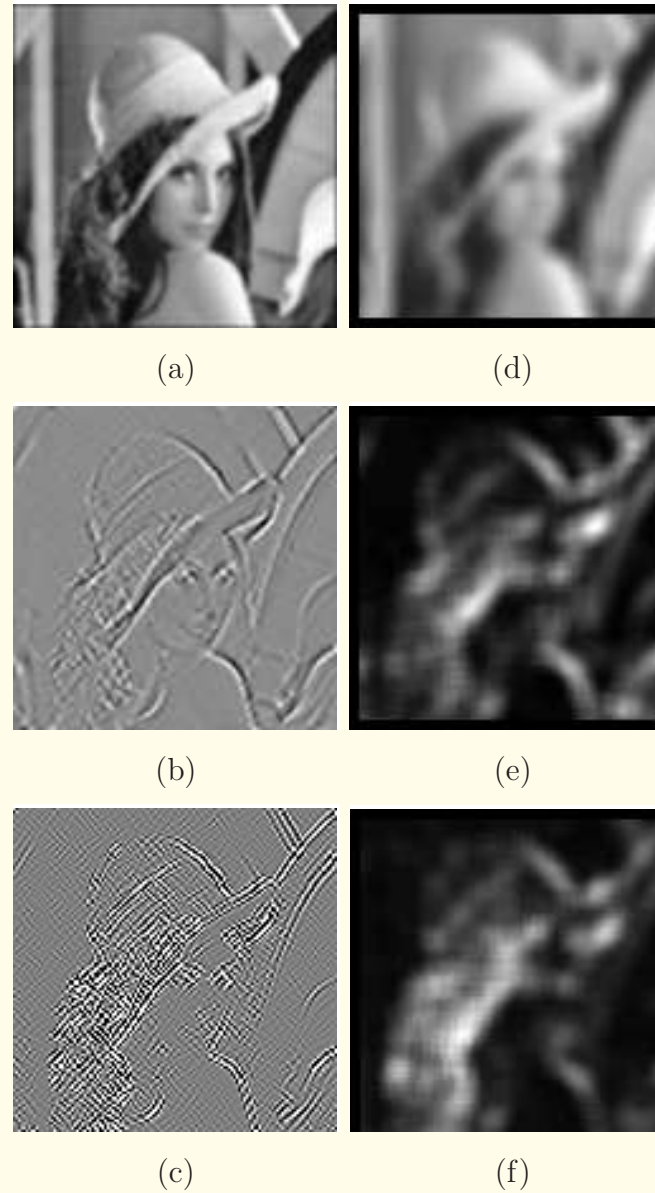


Figure 7.12: Results of convolution of the Lenna test image of size 128×128 pixels using the following 5×5 Laws' operators: (a) $L5L5$, (b) $E5E5$, and (c) $W5W5$. (d) – (f) were obtained by summing the absolute values of the results in (a) – (c), respectively, in a 9×9 moving window, and represent three measures of texture energy. The image in (c) was obtained by mapping the range $[-200, 200]$ out of the full range of $[-1338, 1184]$ to $[0, 255]$.



7.5 Fractal Analysis

Fractals are defined in several different ways.

The most common definition:

a pattern composed of repeated occurrences of a basic unit at multiple scales of detail in a certain order of generation.

The notion of “self-similarity”:

nested recurrence of the same motif at smaller and smaller scales.

The relationship to texture is evident in the property of repeated occurrence of a motif.



Fractal patterns occur abundantly in nature as well as in biological and physiological systems:

the self-replicating patterns of the complex leaf structures of ferns (see Figure 7.13),

the ramifications of the bronchial tree in the lung (see Figure 7.1),

and the branching and spreading (anastomotic) patterns of the arteries in the heart.

Fractals and the notion of chaos are related to the area of nonlinear dynamic systems.



Figure 7.13: The leaf of a fern with a fractal pattern.



7.5.1 *Fractal dimension*

Whereas the self-similar aspect of fractals is apparent in the examples mentioned above, it is not so obvious in other patterns such as clouds, coastlines, and mammograms, which are also said to have fractal-like characteristics.

In such cases, the “fractal nature” perceived is more easily related to the notion of complexity in the dimensionality of the object, leading to the concept of the fractal dimension.



If one were to use a large ruler to measure the length of a coastline, the minor details present in the border having small-scale variations would be skipped, and a certain length would be derived.

If a smaller ruler were to be used, smaller details would get measured, and the total length that is measured would increase (between the same end points as before).



This relationship may be expressed as

$$l(\eta) = l_0 \eta^{1-d_f}, \quad (7.32)$$

where $l(\eta)$ is the length measured

with η as the measuring unit (the size of the ruler),

d_f is the fractal dimension,

and l_0 is a constant.



Fractal patterns exhibit a linear relationship between the log of the measured length and the log of the measuring unit:

$$\log[l(\eta)] = \log[l_0] + (1 - d_f) \log[\eta]; \quad (7.33)$$

the slope of this relationship is related to the fractal dimension d_f of the pattern.

This method is known as the caliper method to estimate the fractal dimension of a curve.

It is obvious that $d_f = 1$ for a straight line.



Fractal dimension is a measure that quantifies how the given pattern fills space.

The fractal dimension of a straight line is unity,

that of a circle or a 2D perfectly planar (sheet-like) object is two,

and that of a sphere is three.

As the irregularity or complexity of a pattern increases, its fractal dimension increases up to its own Euclidean dimension d_E plus one.



The fractal dimension of a jagged, rugged, convoluted, kinky, or crinkly curve will be greater than unity, and reaches the value of two as its complexity increases.

The fractal dimension of a rough 2D surface will be greater than two, and approaches three as the surface roughness increases.

In this sense, fractal dimension may be used as a measure of the roughness of texture in images.



Estimation of the fractal dimension of 1D signals by computing the relative dispersion $RD(\eta)$, defined as the ratio of the standard deviation to the mean, using varying bin size or number of samples of the signal, η :

For a fractal signal, the expected variation of $RD(\eta)$ is

$$RD(\eta) = RD(\eta_0) \left[\frac{\eta}{\eta_0} \right]^{H-1}, \quad (7.34)$$

where η_0 is a reference value for the bin size.



H is the Hurst coefficient, related to the fractal dimension as

$$d_f = d_E + 1 - H. \quad (7.35)$$

$d_E = 1$ for 1D signals, 2 for 2D images, etc.

The value of H , and hence d_f , may be estimated by measuring the slope of the straight-line approximation to the relationship between $\log[RD(\eta)]$ and $\log(\eta)$.



7.5.2 Fractional Brownian motion model

Fractal signals may be modeled in terms of fractional Brownian motion.

The expectation of the differences between the values of such a signal at a position η and another at $\eta + \Delta\eta$ follow the relationship

$$E[|f(\eta + \Delta\eta) - f(\eta)|] \propto |\Delta\eta|^H. \quad (7.36)$$

The slope of a plot of the averaged difference as above versus $\Delta\eta$ (on a log – log scale) may be used to estimate H and the fractal dimension.



Chen et al. applied fractal analysis for the enhancement and classification of ultrasonographic images of the liver.

Burdett et al. derived the fractal dimension of 2D ROIs of mammograms with masses by using the expression in Equation 7.36.

Benign masses, due to their smooth and homogeneous texture, were found to have low fractal dimensions of about 2.38.

Malignant tumors, due to their rough and heterogeneous texture, had higher fractal dimensions of about 2.56.



The PSD of a fractional Brownian motion signal $\Phi(\omega)$ is expected to follow the so-called power law as

$$\Phi(\omega) \propto \frac{1}{|\omega|^{(2H+1)}}. \quad (7.37)$$

The derivative of a signal generated by a fractional Brownian motion model is known as a fractional Gaussian noise signal;

the exponent in the power-law relationship for such a signal is changed to $(2H - 1)$.



7.5.3 Fractal analysis of texture

Based upon a fractional Brownian motion model, Wu et al. defined an averaged intensity-difference measure $id(k)$ for various values of the displacement or distance parameter k as

$$id(k) = \frac{1}{2N(N-k-1)} \left[\sum_{m=0}^{N-1} \sum_{n=0}^{N-k-1} |f(m, n) - f(m, n+k)| \right. \\ \left. + \sum_{m=0}^{N-k-1} \sum_{n=0}^{N-1} |f(m, n) - f(m+k, n)| \right]. \quad (7.38)$$

The slope of a plot of $\log[id(k)]$ versus $\log[k]$ was used to estimate H and the fractal dimension.



Wu et al. applied fractal analysis as well GCM features, Fourier spectral features, gray-level difference statistics, and Laws' texture energy measures for the classification of ultrasonographic images of the liver as normal, hepatoma, or cirrhosis;

accuracies of 88.9%, 83.3%, 80.0%, 74.4%, and 71.1% were obtained.

Lee et al. derived features based upon fractal analysis including the application of multiresolution wavelet transforms.

Classification accuracies of 96.7% in distinguishing between normal and abnormal liver images, and 93.6% in discriminating between cirrhosis and hepatoma were obtained.



Byng et al. describe a surface-area measure to represent the complexity of texture in an image by interpreting the gray level as the height of a function of space; see Figure 7.14.

In a perfectly uniform image of size $N \times N$ pixels, with each pixel being of size $\eta \times \eta$ units of area, the surface area would be equal to $(N\eta)^2$.

When adjacent pixels are of unequal value, more surface area of the blocks representing the pixels will be exposed, as shown in Figure 7.14.



The total surface area for the image may be calculated as

$$\begin{aligned}
 A(\eta) = & \sum_{m=0}^{N-2} \sum_{n=0}^{N-2} \{ \eta^2 \\
 & + \eta [|f_{\eta}(m, n) - f_{\eta}(m, n + 1)| \\
 & + |f_{\eta}(m, n) - f_{\eta}(m + 1, n)|] \}, \quad (7.39)
 \end{aligned}$$

where $f_{\eta}(m, n)$ is the 2D image expressed as a function of the pixel size η .



To estimate the fractal dimension of the image, we could derive several smoothed and downsampled versions of the given image (representing various scales η), and estimate the slope of the plot of $\log[A(\eta)]$ versus $\log[\eta]$;

the fractal dimension is given as two minus the slope.

A perfectly uniform image would demonstrate no change in its area, and have a fractal dimension of two;

images with rough texture would have increasing values of the fractal dimension, approaching three.



Yaffe et al. obtained fractal dimension values in the range of $[2.23, 2.54]$ with 60 mammograms.

Byng et al. demonstrated the usefulness of the fractal dimension as a measure of increased fibroglandular density in the breast, and related it to the risk of development of breast cancer.

Fractal dimension was found to complement histogram skewness (see Section 7.3) as an indicator of breast cancer risk.

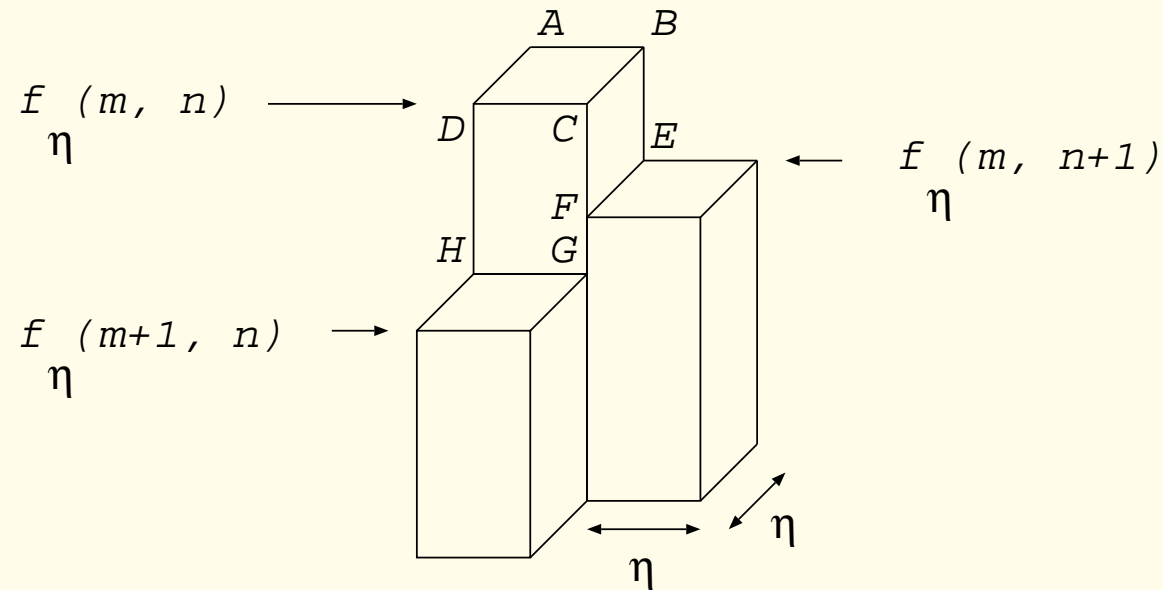


Figure 7.14: Computation of the exposed surface area for a pixel $f(m, n)$ with respect to its neighboring pixels $f(m, n+1)$ and $f(m+1, n)$. A pixel at (m, n) is viewed as a box (or building) with base area $\eta \times \eta$ and height equal to the gray level $f(m, n)$. The total exposed surface area for the pixel $f(m, n)$, with respect to its neighboring pixels at $(m, n+1)$ and $(m+1, n)$, is the sum of the areas of the rectangles $ABCD$, $CBEF$, and $DCGH$.



7.5.4 Applications of fractal analysis

Lundahl et al. estimated the values of H from scan lines of X-ray images of the calcaneus (heel) bone.

The value was decreased by injury and osteoporosis, indicating reduced complexity of structure as compared to normal bone.

Esgiar et al. found the fractal dimension to complement the GCM texture features of entropy and correlation in the classification of tissue samples from the colon:

the inclusion of fractal dimension increased the sensitivity from 90% to 95%, and the specificity from 86% to 93%.

(See the book for more details.)



7.6 Fourier-domain Analysis of Texture

The Fourier spectrum of an image with random texture contains the spectral characteristics of the spot involved in its generation

(according to the spot-noise model shown in Figure 7.4).

The effects of multiplication with the spectrum of the random-noise field (which is essentially, and on the average, a constant) may be removed by smoothing operations.

Thus, the important characteristics of the texture are readily available in the Fourier spectrum.



The Fourier spectrum of an image with periodic texture includes not only the spectral characteristics of the spot, but also the effects of multiplication with the spectrum of the impulse field involved in its generation.

The Fourier spectrum of a train of impulses in 1D is a discrete spectrum with a constant value at the fundamental frequency (the inverse of the period) and its harmonics.

In 2D, the Fourier spectrum of a periodic field of impulses is a periodic field of impulses.

Multiplication of the Fourier spectrum of the spot with that of the impulse field causes modulation of the intensities in the former, leading to bright regions at regular intervals.



With real-life images, the effects of windowing or finite data, as well as of quasi-periodicity, will lead to smearing of the impulses in the spectrum of the impulse field involved.

Regardless, the spectrum of the image may be expected to demonstrate a field of bright regions at regular intervals.

The information related to the spectra of the spot and the impulse field components may be derived from the spectrum of the textured image by averaging in the polar-coordinate axes.



Let $F(r, t)$ be the polar-coordinate representation of the Fourier spectrum of the given image;

in terms of the Cartesian frequency coordinates (u, v) , we have

$$r = \sqrt{u^2 + v^2}, \text{ and } t = \arctan(v/u).$$

Derive the projection functions in r and t by integrating $F(r, t)$ in the other coordinate as

$$F(r) = \int_{t=0}^{\pi} F(r, t) dt, \quad (7.40)$$

$$F(t) = \int_{r=0}^{r_{\max}} F(r, t) dr. \quad (7.41)$$



The averaging effect of integration as above leads to improved visualization of the spectral characteristics of periodic texture.

Quantitative features may be derived from $F(r)$ and $F(t)$ or directly from $F(r, t)$ for pattern classification purposes.



Jernigan and D'Astous used the normalized PSD values within selected frequency bands as PDFs, and computed entropy values.

It was expected that structured texture would lead to low entropy (due to spectral bands with concentrated energy)

and random texture would lead to high entropy values (due to a uniform distribution of spectral energy).

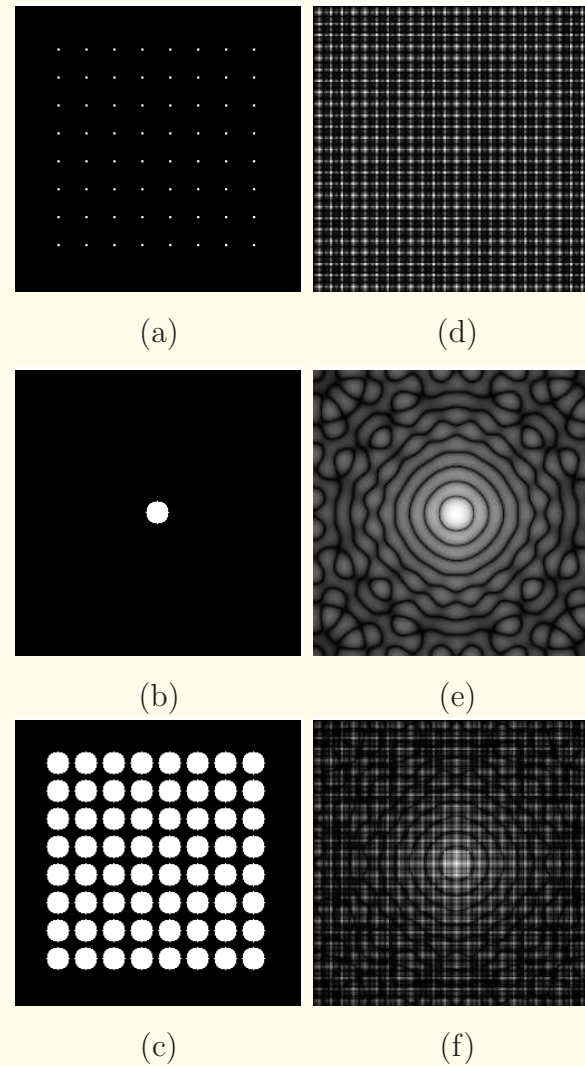


Figure 7.15: Fourier spectral characteristics of periodic texture generated using the spot-noise model in Figure 7.4. (a) Periodic impulse field. (b) Circular spot. (c) Periodic texture generated by convolving the spot in (b) with the impulse field in (a). (d) – (f) Log-magnitude Fourier spectra of the images in (a) – (c), respectively.

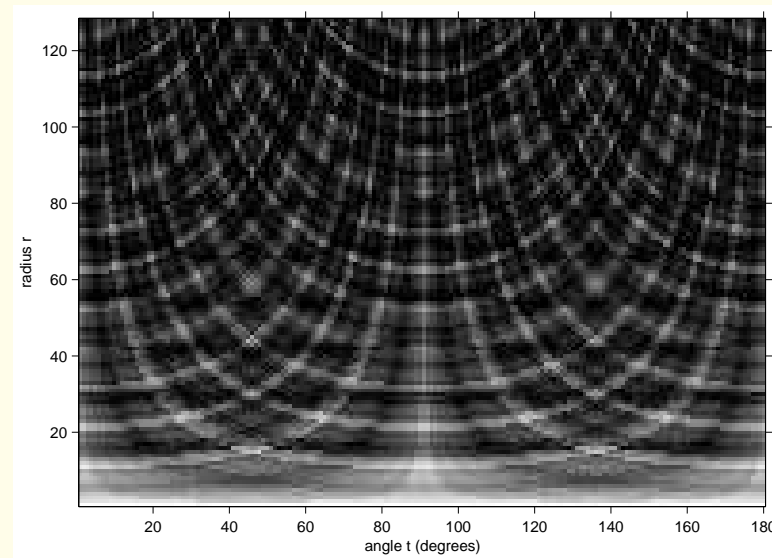
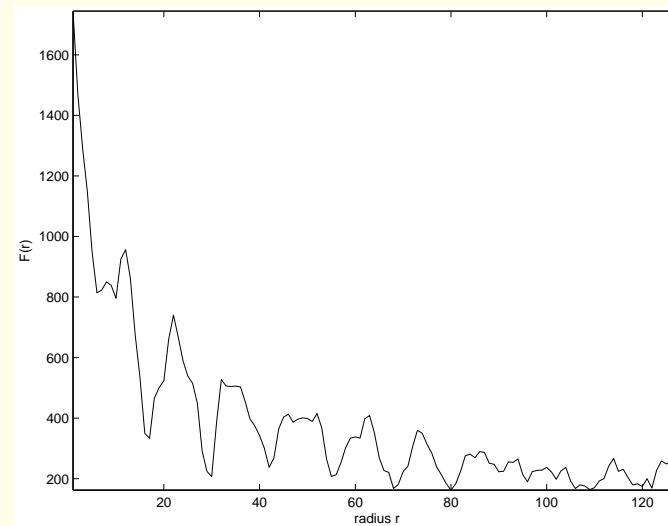
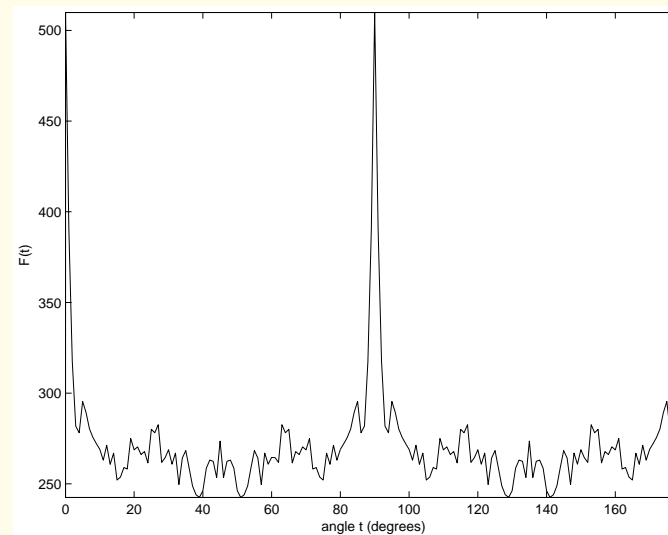


Figure 7.16: The spectrum in Figure 7.15 (f) converted to polar coordinates; only the upper half of the spectrum was mapped to polar coordinates.

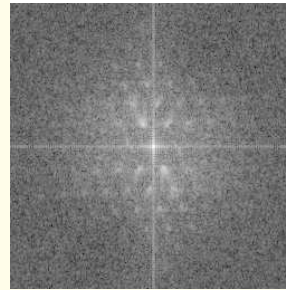


(a)

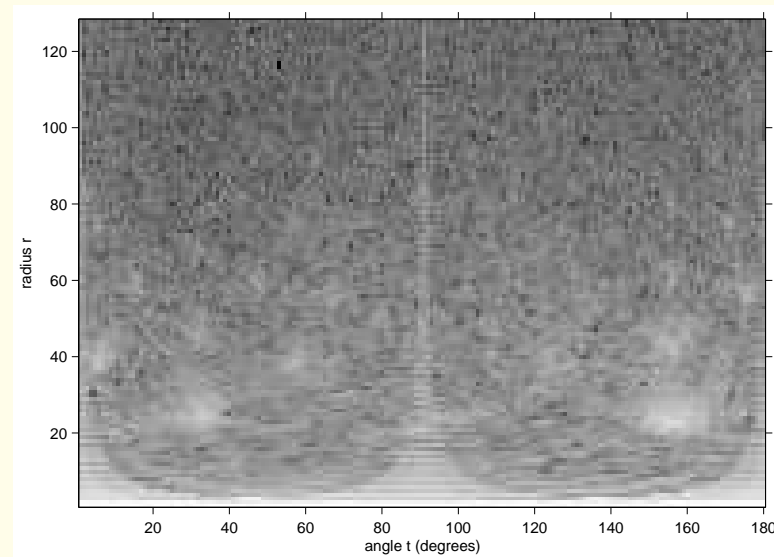


(b)

Figure 7.17: Projection functions in (a) the radial coordinate r , and (b) the angle coordinate t obtained by integrating (summing) the spectrum in Figure 7.16 in the other coordinate.

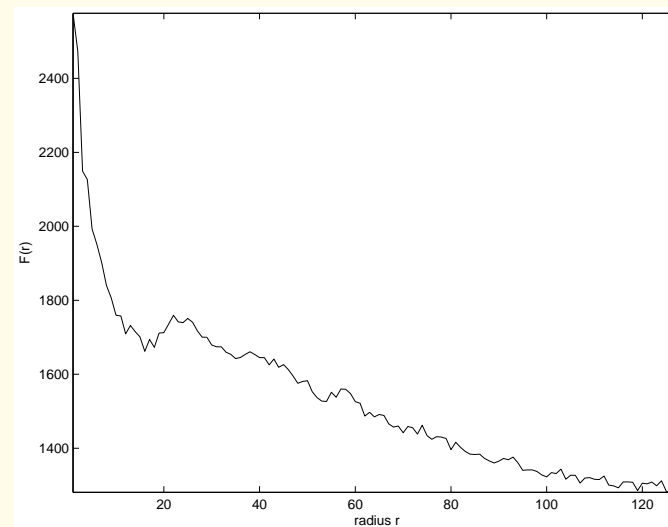


(a)

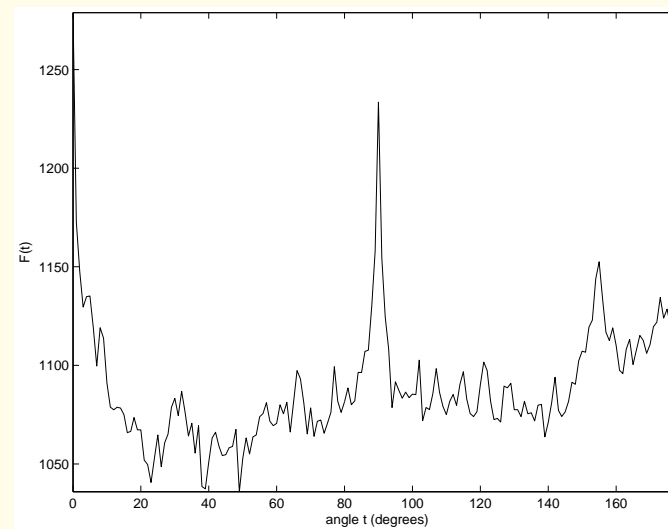


(b)

Figure 7.18: Fourier spectral characteristics of the quasi-periodic texture of the fly's eye image in Figure 7.3 (b): (a) The Fourier spectrum in Cartesian coordinates (u, v) . (b) The upper half of the spectrum in (a) mapped to polar coordinates.

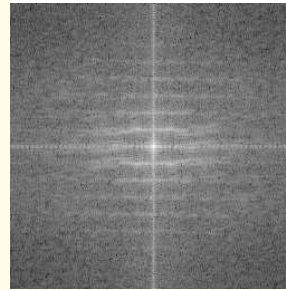


(a)

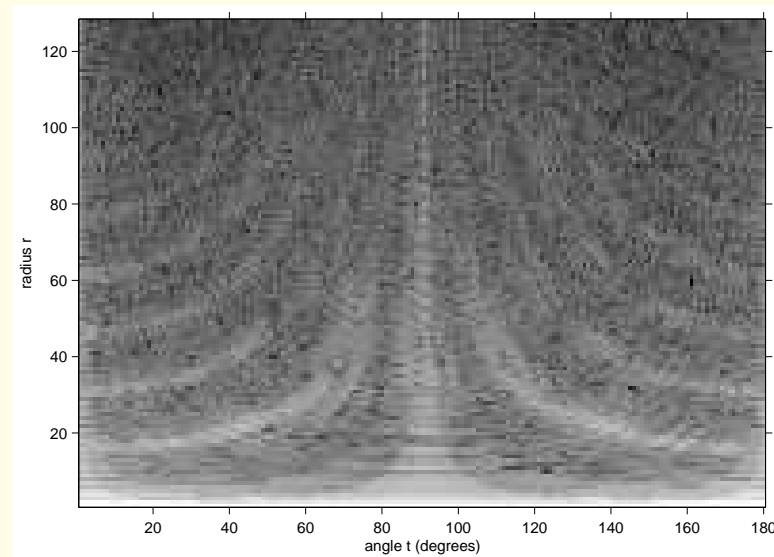


(b)

Figure 7.19: Projection functions in (a) the radial coordinate r , and (b) the angle coordinate t obtained by integrating (summing) the spectrum in Figure 7.18 (b) in the other coordinate.

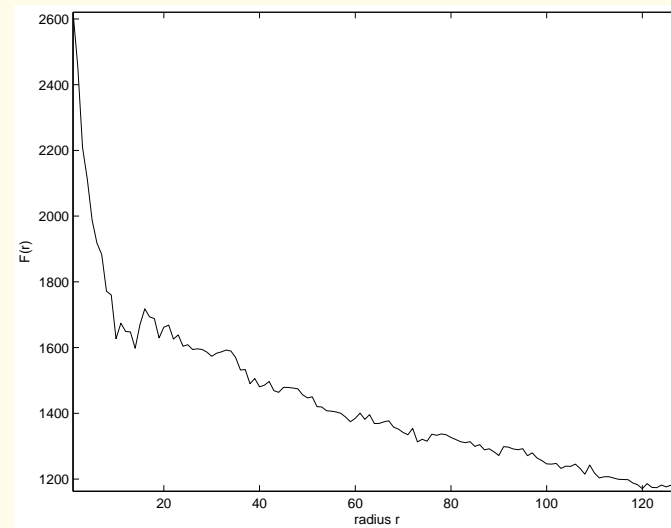


(a)

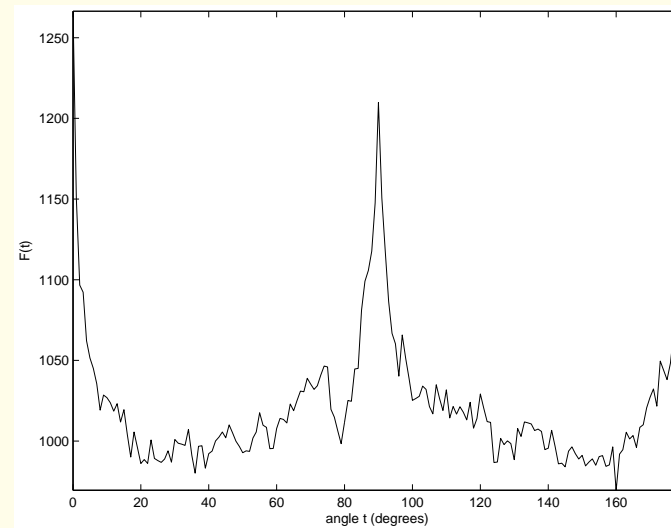


(b)

Figure 7.20: Fourier spectral characteristics of the ordered texture of the snake-skin image in Figure 7.3 (c): (a) The Fourier spectrum in Cartesian coordinates (u, v) . (b) The upper half of the spectrum in (a) mapped to polar coordinates.



(a)



(b)

Figure 7.21: Projection functions in (a) the radial coordinate r , and (b) the angle coordinate t obtained by integrating (summing) the spectrum in Figure 7.20 (b) in the other coordinate.



Bovik discussed multichannel narrow-band filtering and modeling of texture.

Highly granular and oriented texture may be expected to present spatio-spectral regions of concentrated energy.

Gabor filters may then be used to filter, segment, and analyze such patterns.



7.7 Segmentation and Structural Analysis of Texture

See the book for details.

7.7.1 Homomorphic deconvolution of periodic patterns

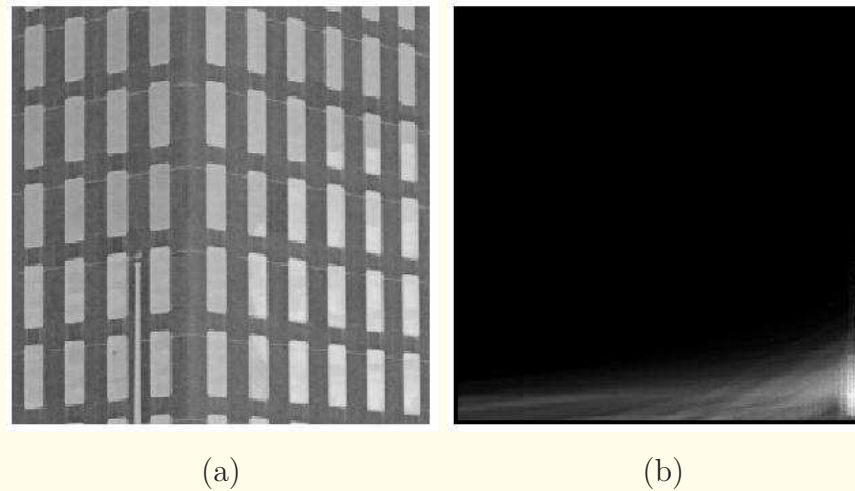


Figure 7.22: (a) An image of a part of a building with a periodic arrangement of windows. (b) A single window structure extracted by homomorphic deconvolution. Reproduced with permission from A.C.G. Martins and R.M. Rangayyan, “Texture element extraction via cepstral filtering in the Radon domain”, *IETE Journal of Research (India)*, 48(3,4): 143 – 150, 2002. © IETE.

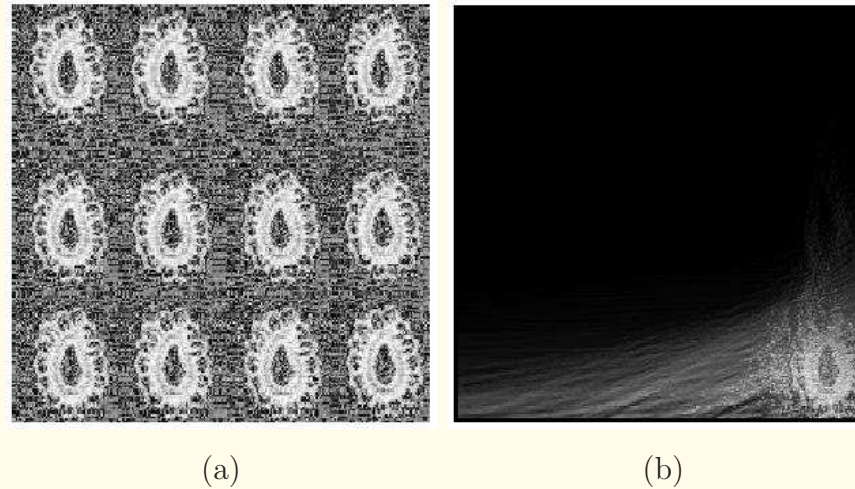


Figure 7.23: (a) An image with a periodic arrangement of a textile motif. (b) A single motif or texton extracted by homomorphic deconvolution. Reproduced with permission from A.C.G. Martins and R.M. Rangayyan, “Texture element extraction via cepstral filtering in the Radon domain”, *IETE Journal of Research* (India), 48(3,4): 143 – 150, 2002. © IETE.



7.8 Audification and Sonification of Texture in Images

See the book for details.



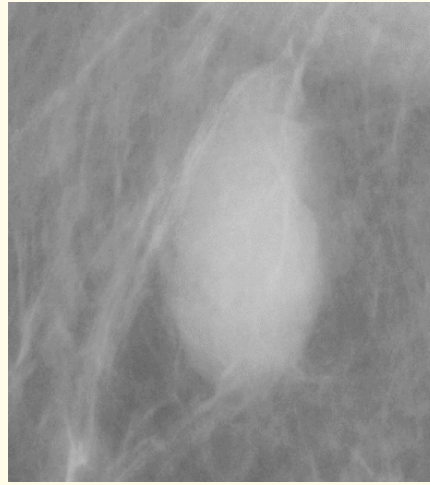
7.9 Application: Analysis of Breast Masses

7.9.1 *Adaptive normals and ribbons around mass margins*

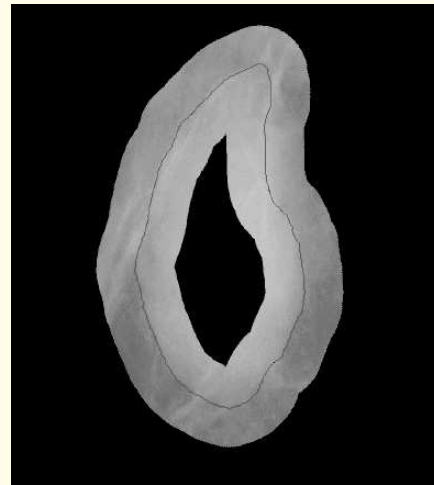
7.9.2 *Gradient and contrast measures*

7.9.3 *Results of pattern classification*

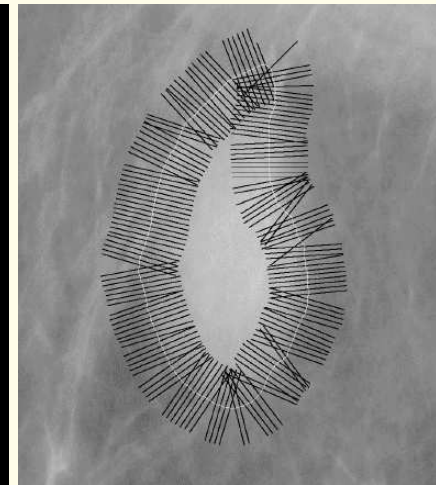
See the book for details.



(a)



(b)

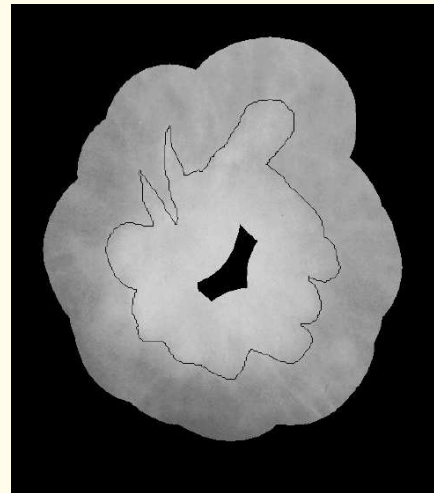


(c)

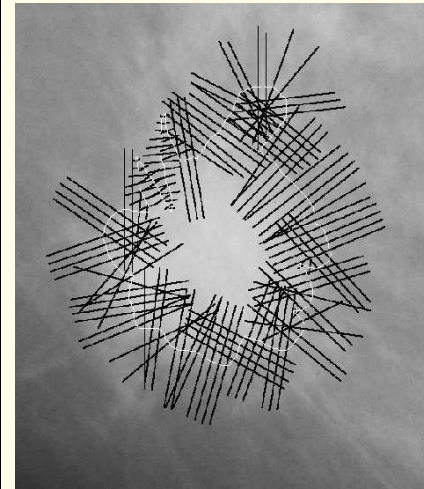
Figure 7.24: (a) A $1,000 \times 900$ section of a mammogram containing a circumscribed benign mass. Pixel size = $50 \mu m$. (b) Ribbon or band of pixels across the boundary of the mass extracted by using morphological operations. (c) Pixels along the normals to the boundary, shown for every tenth boundary pixel. Maximum length of the normals on either side of the boundary = 80 pixels or $4 mm$. Images courtesy of N.R. Mudigonda.



(a)



(b)



(c)

Figure 7.25: (a) A 630×560 section of a mammogram containing a spiculated malignant tumor. Pixel size = $50 \mu m$. (b) Ribbon or band of pixels across the boundary of the tumor extracted by using morphological operations. (c) Pixels along the normals to the boundary, shown for every tenth boundary pixel. Maximum length of the normals on either side of the boundary = 80 pixels or $4 mm$. Images courtesy of N.R. Mudigonda.

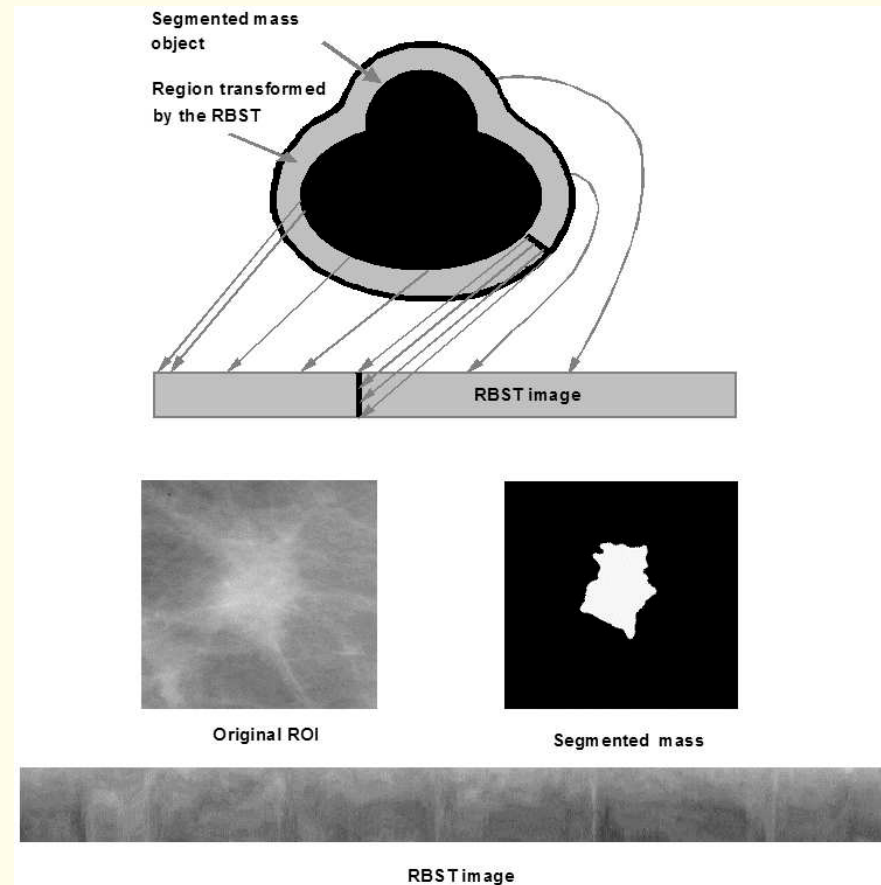


Figure 7.26: Mapping of a ribbon of pixels around a mass into a rectangular image by the rubber-band straightening transform. Figure courtesy of B. Sahiner, University of Michigan, Ann Arbor, MI. Reproduced with permission from B.S. Sahiner, H.P. Chan, N. Petrick, M.A. Helvie, and M.M. Goodsitt, “Computerized characterization of masses on mammograms: The rubber band straightening transform and texture analysis”, *Medical Physics*, 25(4): 516 – 526, 1995. © American Association of Medical Physicists.



